J Mater Sci

Metals & corrosion

Effect of process parameters on tensile and impact strength properties of AISI 316L stainless steel fabricated via laser-powder bed fusion

C. Morales[1,*], A. Fortini[1], C. Soffritti[1], M. Actis Grande[2], M. Gragnanini[1], and M. Merlin[1]

[1] *Department of Engineering (DE), University of Ferrara, Via Saragat 1, 44122 Ferrara, Italy*
[2] *Department of Applied Science and Technology (DISAT), Polytechnic of Turin, Viale T. Michel 5, 15121 Alessandria, Italy*

Received: 22 July 2025
Accepted: 16 November 2025

ABSTRACT

Recent advances in the production of metallic components via Laser-Powder Bed Fusion (L-PBF) have attracted considerable interest, promising to achieve properties comparable to those of conventional manufacturing while reducing production time and costs. Among the materials suitable for L-PBF, austenitic stainless steels, such as the AISI 316L one, stand out due to their versatility across various industrial applications. The selection of process parameters including laser power, hatch spacing, scan speed and layer thickness strongly influences the final properties of printed parts. The present work aims to evaluate the metallurgical and mechanical features of L-PBF AISI 316L samples produced with different layer thicknesses (25, 50 and 100 μm) and according to two building directions, i.e., horizontal (xy) and vertical (xz) with respect to the building platform. Experimental investigations including density measurements, microstructural analyses through optical and scanning electron microscopes, tensile and instrumented Charpy impact tests were performed. The relationship between the employed layer thickness and both tensile strength and impact toughness was also assessed. By selecting proper process parameters such as laser power, scanning speed and layer thickness within a specific range of values, the resulted laser density energies promote good-quality of the printed samples with excellent mechanical properties.

Handling Editor: Sophie Primig.

Address correspondence to E-mail: mrlcdy@unife.it

https://doi.org/10.1007/s10853-025-11895-2
Published online: 02 December 2025

GRAPHICAL ABSTRACT

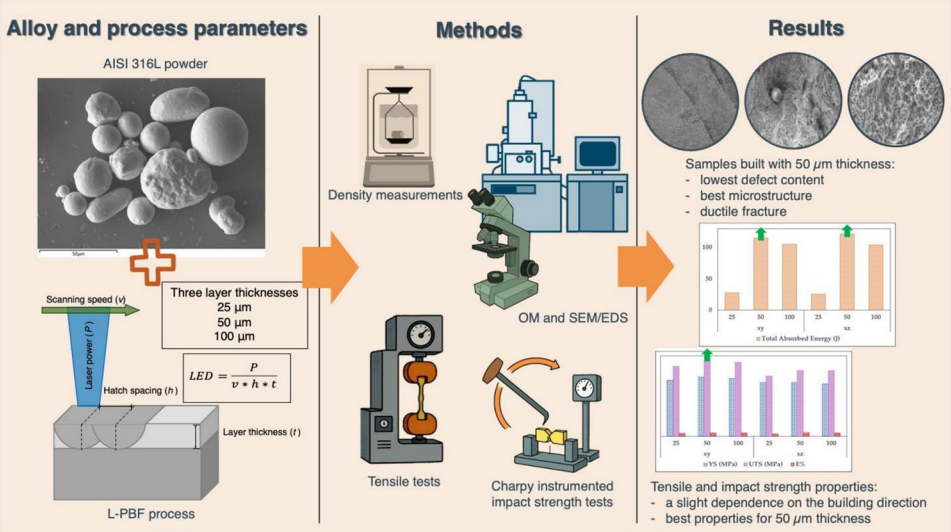

Introduction

Additive Manufacturing (AM), also known as 3D printing, has shown remarkable potential for fabricating complex parts across a wide range of metallic materials. Beyond design flexibility, AM techniques are also material-efficient, as they generate significantly less waste compared to traditional subtractive manufacturing processes. In recent years, Powder Bed Fusion (PBF) and Directed Energy Deposition techniques have gained prominence owing to their great flexibility in producing high-quality components, especially complex parts with short lead times. Among these, the Laser-Powder Bed Fusion (L-PBF) is one of the earliest and most versatile AM techniques, widely employed to fabricate metallic parts starting from powders of different materials [1–3]. This process employs a laser as a heat source to selectively melt the powder bed layer by layer, ultimately yielding a fully dense metallic part [1, 4, 5]. A broad spectrum of alloys, including aluminum alloys [6–8], steels [9–11], titanium alloys [12, 13], as well as cobalt and high-resistant alloys [14–17], has been successfully processed by L-PBF. Within the steel family, AISI 316L austenitic stainless steel has received particular attention due to its widespread applications, especially in the automotive [18] and biomedical fields [19], where its combination of mechanical strength and corrosion resistance represents a key asset [20–24].

Considerable efforts have been dedicated to optimizing the L-PBF process parameters to produce high-quality AISI 316L parts, with a particular attention to the effect of laser energy density (LED), laser power, scanning strategy, layer thickness and building direction [25–28] on mechanical and microstructural properties [29, 30]. Peng and Chen [31] investigated the effect of LED on AISI 316L samples processed by L-PBF, keeping the layer thickness constant at 50 µm, while varying LED between 36 and 48 J/cm^3. Their findings indicated that higher laser power and scanning speed improved melt pool stability and increased material density, with the highest relative density of 98.87% obtained at a LED of 48.48 J/cm^3. In contrast, Choi et al. [32] explored LED values ranging from 10 to 1000 J/mm^3, focusing on their impact on densification behavior and microstructural evolution of AISI 316L samples fabricated via L-PBF. Their results highlighted that LED values below 50 J/mm^3 made the printed parts more prone to crack formation, hindering samples' densification. Conversely, LED values around 200 J/mm^3 led to an increase in porosity content. Ho-Jin Lee [33] studied the effect of different LED values on microstructural defects, tensile properties and hardness of AISI 316L components produced via L-PBF. By varying combinations of laser power, scanning speed and hatch distance, the author highlighted the mutual effect of such parameters on LED values. Experimental results revealed that the highest tensile strengths were obtained for the highest LED values (around 155 J/mm^3), even though the best

Table 1 Nominal chemical composition (wt. %) of the AISI 316L powder

Element	C	Mn	Si	Cr	Ni	P	Mo	Fe
	0.03	2.0	1.0	16.5 – 18.5	8.0 – 13.0	0.04	2.0 – 2.2	Balance

apparent density and lowest porosity were achieved at a lower LED value (79 J/mm^3). Tucho et al. [34] found that the range of LED values between 50 and 80 J/mm^3 was effective in improving hardness and reducing porosity, thereby enhancing densification of AISI 316L steel parts. In addition to LED, several authors have emphasized the role of layer thickness in determining the quality and density of L-PBF AISI 316L samples [30, 35, 36]. Hyer et al. [37] examined thicknesses of 40, 80 and 120 µm, demonstrating that the porosity increased with layer thickness, with 40 µm providing the best results for improving the density of the material. In addition, Dabwan et al. [38] focused on the effect of four different layer thicknesses on the post-processing surface quality of L-PBF AISI 316L steel using a specific milling process. The results showed that samples printed with 60 µm of layer thickness exhibited the most notable improvements in surface integrity. Based on the above-mentioned literature, a deep investigation on the role of laser and powder-related parameters, i.e., layer thickness and LED is crucial for optimizing the microstructural and mechanical behavior of L-PBF AISI 316L steel. Although prior studies focused on exploring the role of the process parameters on the tensile and fatigue properties of L-PBF AISI 316L steels [26, 39–43], only a few have addressed how the parameters influence the impact behavior of the material [42, 44, 45]. Particularly, Afkhami et al. [42] investigated the effect of the L-PBF process parameters variation and post-processing treatments on the impact behavior of AISI 316L printed samples: notched and un-notched Charpy specimens were tested according to different building directions. From the results, the authors found that the building direction does not cause a strong effect on the impact properties of the material; however, they demonstrated that the process parameters affect significantly the impact toughness, and the best results were obtained for samples fabricated with the highest density values. Wang et al. [45] focused on the impact behavior of AISI 316L notched Charpy samples drawn along three different crystallographic directions from as-built prisms fabricated with constant process parameters. With respect to these crystallographic directions, the authors compared the total absorbed energies of the material at both room and cryogenic temperature. De Sonis et al. [44] evaluated the impact toughness of AISI 316L samples, manufactured with a L-PBF 3D printer perpendicular to building platform, at both room and cryogenic temperature. The samples were fabricated with constant processing parameters and tested by using an instrumented Charpy pendulum considering the effect of three different heat treatment parameters.

In the light of this, the novelty of the present study lies in evaluating the effect of three different sets of parameters—and consequently of the adopted best laser power, scanning speed and hatch spacing to print the material—on the instrumented impact strength of L-PBF AISI 316L samples. V-notched Charpy specimens were drawn from parallelepiped samples fabricated along both perpendicular and parallel directions with respect to the building platform. An instrumented pendulum was used to calculate not only the total absorbed energy but also the two complementary contributions of the initiation energy and the propagation energy, as well as the peak force and the displacement at the peak force. For a comprehensive mechanical assessment, tensile tests were also performed on samples fabricated according to both parallel and perpendicular directions with respect to the building platform and all the mechanical properties were correlated to the three different sets of process parameters. Moreover, cubic samples were fabricated to carry out a specific focus on the effect of the different layer thicknesses on the apparent density and on the microstructure affecting the mechanical properties. Fractographic investigations were performed by scanning electron microscopy (SEM) on the fracture surfaces of tensile and Charpy specimens to study how the microstructural features influenced the fracture path during crack propagation, thus emphasizing the importance of an optimization of the process parameters.

Experimental procedure

Gas-atomized AISI 316L powder, supplied by GE Additive (GE Additive, Ohio, USA) and with nominal chemical composition detailed in Table 1, was used to produce L-PBF samples by a M2 Cusing machine (GE Additive) equipped with a 400 W Ytterbium-doped fiber laser and employing pure nitrogen for the environment protection of the build chamber. The particle morphology

was analyzed by a Zeiss EVO MA15 scanning electron microscope (Carl Zeiss, Oberkochen, Germany) equipped with an Oxford Xmax 50 microprobe (Oxford Instruments, Abingdon-on-Thames, UK) for energy-dispersive spectroscopy (SEM/EDS) and following the procedure described in the ASTM E2651-13 standard [46]. A small amount of powder particles was dispersed in ethanol using a Beta 1895 ultrasonic cleaning machine (Beta Utensili, Sovico, Monza e Brianza, Italy), deposited onto a conductive sample holder, and then observed via SEM/EDS. The SEM micrographs in Fig. 1 show the spherical morphology of the AISI 316L powder particles (Fig. 1a), some small, scattered satellites (Fig. 1b) and a particle size plot which shows the cumulative frequency distribution of the particle sized with 90% of the powder particle size below 20 μm ($D90 = 19.4$ μm) in Fig. 1c.

In this study, three different layer thicknesses—25 μm, 50 μm and 100 μm—were considered to fabricate three different sets of samples: adjusting the other parameters laser power, the scanning speed and the hatch spacing according to good practice. The normalized process parameters, as well as the calculated LED values, are summarized in Table 2. For samples with a layer thickness of 50 μm, the process parameters, i.e., hatch spacing, scanning speed, and laser power were directly provided by the powder supplier. For each thickness, six parallelepiped samples measuring 20 × 10 × 200 mm in size and six other parallelepipeds measuring 12 × 12 × 59 mm were fabricated to perform tensile and impact strength tests, respectively. To systematically evaluate the mechanical anisotropy inherent to the L-PBF process, specimens were fabricated in two orthogonal building directions: horizontal (*xy*, parallel to the building platform) and vertical (*xz*, perpendicular to the building platform). Half of the tensile and impact specimens were printed perpendicularly to the building platform (vertical, *xz*), while the rest were printed parallelly to the same platform (horizontal, *xy*). This experimental design enables direct comparison of properties along and perpendicular to the predominant grain growth direction, thereby quantifying the degree of anisotropy introduced by the layer-by-layer solidification process. Additionally, six cubic samples measuring 10 × 10 × 10 mm were fabricated for each job to perform apparent density measurements. Figure 2 shows the printing layout of the samples on the building

Table 2 Normalized process parameters used for the fabrication of the three sets of samples

Normalized process parameter	Layer thickness *(t)* [μm]		
	25	*50**	100
Laser energy density *(LED)*** [J/mm^3]	80	55	44
Hatch spacing *(h)* [mm]	0.1	0.1	0.1
Scanning speed *(v)* [mm/s]	600	900	567
Laser power *(P)* [J/s]	120	247	247

* Directly suggested by the powder supplier

** Calculated as P/(v • h • t), in agreement with [47]

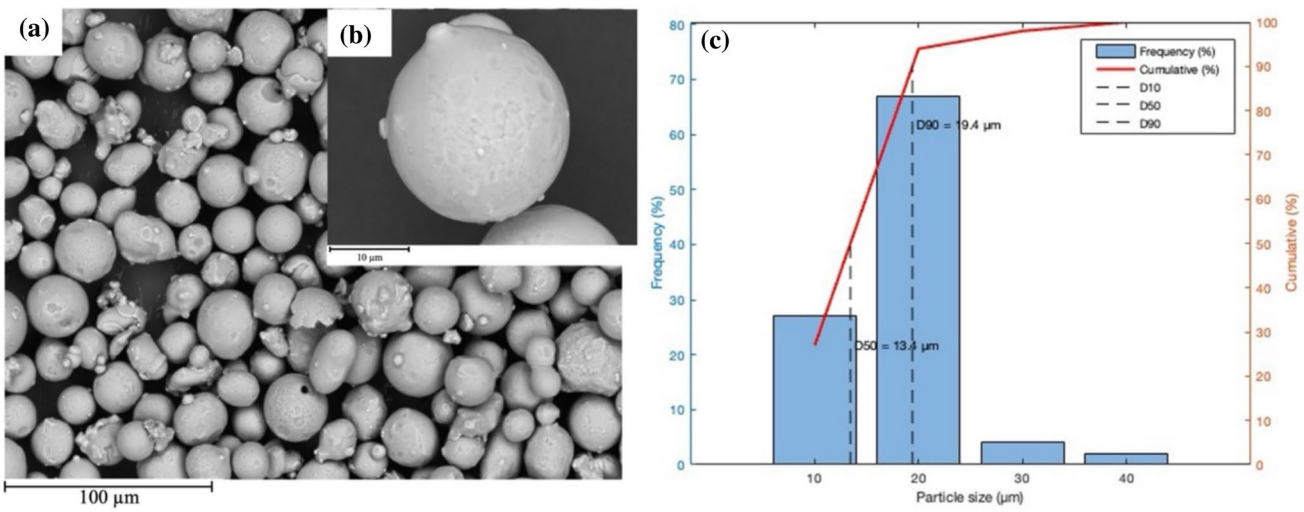

Figure 1 SEM micrographs showing (**a**) an overview of the AISI 316L powder particles with spherical morphology, (**b**) the details of small and dispersed satellite defects and (**c**) frequency powder particle size distribution plot of the AISI 316 L particles.

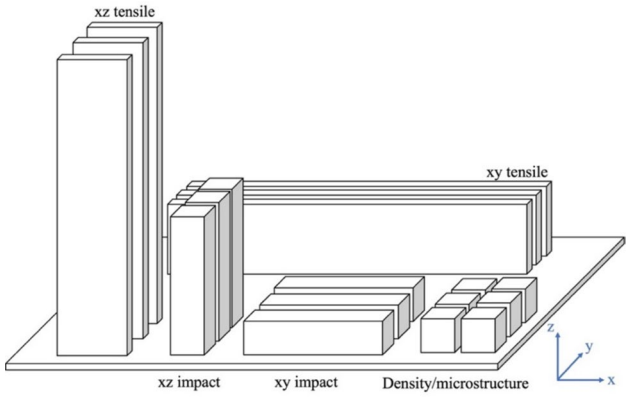

Figure 2 Printing layout of samples on the building platform.

platform. The parallelepipeds intended for impact testing were machined to obtain V-notched samples measuring 10 × 10 × 55 mm, in accordance with the UNI EN ISO 148-1 standard [48]. Impact tests were performed by a Zwick Roell RKP 450 instrumented impact pendulum (Zwick Roell, Genova, Italy). This equipment directly measured the total absorbed energy, from which the two complementary contributions of initiation and propagation energies were obtained in agreement with the ISO 14556:2023 standard [49]. Samples for tensile tests were machined according to the ASTM E8/E8M-2 standard [50]. The static mechanical properties of the steel, namely Young's Modulus (E), yield strength (YS), ultimate tensile strength (UTS) and elongation at fracture (A%) were measured using an Instron 4467 universal testing machine (Instron, Pianezza, Turin, Italy).

The apparent density (ρ) of the material was evaluated using the Archimedes method in agreement with the ASTM B962-08 standard [51]. The weight of each density specimen was recorded three times in air and in distilled water to determine the displaced volume, using a METTLER AE 240 analytical balance (Mettler Toledo, Columbus, OH, USA), recording the weight of the support submerged in distilled water as well. The cubic samples were also used for microstructural analyses on their longitudinal sections (perpendicular to the building platform) and cross sections (parallel to the building platform). All sections underwent standard metallographic preparation in agreement with the ASTM E3-11 standard [52], including mounting in conductive resin, grinding with silicon carbide (SiC) abrasive papers of various grit (from 120 to 1200), polishing with monocrystalline diamond solutions of various grit sizes (from 6 to 1 μm) and final polishing with a colloidal silica suspension of 0.025 μm. After preparation, electrolytic etching was then performed using a 10% oxalic acid solution at 6 V for 30 s. The microstructure was observed using a Leica DMi8 A optical microscope (OM) (Leica, Wetzlar, Germany) and by the same scanning electron microscope, operating in secondary electron imaging mode (SEI-SEM). After impact tests, macrofractographic analyses of fracture surfaces were carried out by a Leica MZ6 stereomicroscope (Leica) to evaluate the lateral expansions of the specimens, according to the three different layer thicknesses. Finally, microfractographic observations of the fracture surfaces of tensile and impact samples were conducted by SEM to identify the main fracture micromechanisms.

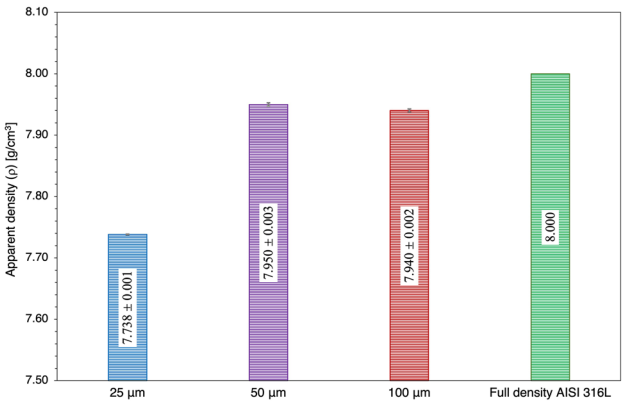

Figure 3 Mean apparent densities for the different layer thicknesses: the full density value of the AISI 316L is reported as a reference.

Results and discussion

Density measurements and microstructural characterization

The mean apparent densities (ρ) of the cubic samples in as-built condition were measured for each set of process parameters and are summarized in Fig. 3. These values were compared with the theoretical full density value of AISI 316L steel assumed as 8.000 g/cm^3 [5]. The results indicated slight variations in the mean apparent density with layer thickness:—of approximately 3%—for the samples fabricated with 25 μm. This reduction may be attributed to the energy per unit volume used for fabricating these specimens.

The increase in LED values may alter strongly the melt pool dynamics, thus promoting the formation of irregular pores or keyhole defects and affecting both the microstructure and properties of the final parts [53, 54]. High LED values are known to refine grain structures and improve homogeneity of the microstructure, however, increase the risk of defect formation due to remelting of the melt pool boundaries, such as lack-of-fusion or gas-induced porosity [55]. Hence, in the case of the 25 μm layer thickness, the adopted LED value probably reduced the apparent density. Conversely, the mean apparent density of the samples fabricated with 50 μm and 100 μm layer thicknesses approached the full density of AISI 316L stainless steel. This outcome is likely due to the LED reduction, that provide sufficient energy for the proper powder fusion without inducing excessive remelting and thus lowering the content of irregular-shaped porosities (as confirmed by the optical microscopy investigations in the following section). The current mean apparent density data were consistent with those previously reported for AISI 316L steel manufactured by L-PBF [5, 28, 56]. Specifically, Liverani et al. [5] used LED values around 100 J/mm^3 achieving relative densities above 98% within a narrow range of laser power (190–150 W) and scanning speed (500–900 mm/s). However, the authors did not investigate the influence of layer thickness. Pragana et al. [28] achieved even higher densities (> 99.6%) using argon shielding and LEDs between 70 and 80 J/mm^3, reinforcing the importance of atmosphere and energy balance. Meanwhile, Bakhtiarian et al. [56] highlighted the synergistic influence of multiple process parameters, including layer thickness, in driving porosity evolution.

The mean values of (ρ) are also linked to the presence of different types of defects within the as-built microstructure such as gas porosity, keyhole porosities, lack of fusion (LoF) and unmelted powder [57]. Representative OM micrographs in Fig. 4 show some defects detected in the longitudinal section and cross section of the cubic samples fabricated with the different layer thicknesses and corresponding LED values. Consistent with previous studies [38, 58–61], the formation of such defects is largely governed by the selection and control of key process parameters. Indeed, appropriate tuning of laser power, scanning speed, hatch spacing and layer thickness is essential to minimize defects occurrence and ensure high-quality L-PBF parts, as mentioned by [62]. As shown in Fig. 4a, b, samples produced with a 25 μm layer thickness, which corresponds to the highest LED, exhibited the highest concentration of internal defects, including irregular gas porosities and LoF. This outcome is due to the high localized energy input, which causes melt pool instability and potential vaporization effects that promote voids. Conversely, samples fabricated using higher layer thicknesses (50 μm in Fig. 4c, d and 100 μm in Fig. 4e, f), associated to lower LED values, exhibited the fewest number of defects. Several studies [37, 38, 63] have confirmed that optimized layer thicknesses (typically in the range of 50–80 μm) and suitable LED values (in the range of 30–60 J/mm^3) promote stable melt pools and enhance layer bonding while reducing the LoF defects as well. This improvement is attributed to better solidification conditions, which are promoted by high heat accumulation during the layer-by-layer building process. Nevertheless, in samples fabricated with the highest layer thickness (Fig. 4e–f), isolated large gas pores and cavities persist, likely due to evaporation phenomena of volatile elements and/or gas entrapment during the L-PBF process [64–66]. Overall, these findings highlight that the defect presence and the morphology of defects are not solely governed by layer thickness, but by the synergic effect of process parameters that are combined in the calculated LED value.

After electrolytic etching, the microstructure was examined along the longitudinal and cross sections (Figs. 5 and 6, respectively). OM micrographs in Fig. 5a–c reveal elongated melt pools, indicative of the scanning patterns selected for building the samples. At higher magnification (Fig. 5d–f), a dendritic cellular microstructure is visible within these pools, consistent with what was previously reported in [67, 68]. The formation of such cellular dendrites is characteristic of rapid solidification during L-PBF and results from steep thermal gradients and high cooling rates. Conversely, with reference to the longitudinal section, the OM micrographs in Fig. 6a–c show the typical semicircular morphology of the melt pools. By comparing the micrographs in Fig. 6a–c, the size of these pools seems to progressively increase from the 25 μm layer thickness to the 100 μm one. This trend reflects the interaction between energy input and deposited material layer by layer; as the layer thickness increases, the melt pool expands to accommodate the greater material volume, even at lower LED values. Moreover, at higher magnification (Fig. 6d–f) differences in size of the dendritic cellular microstructure may be observed with the increasing of layer thickness due to

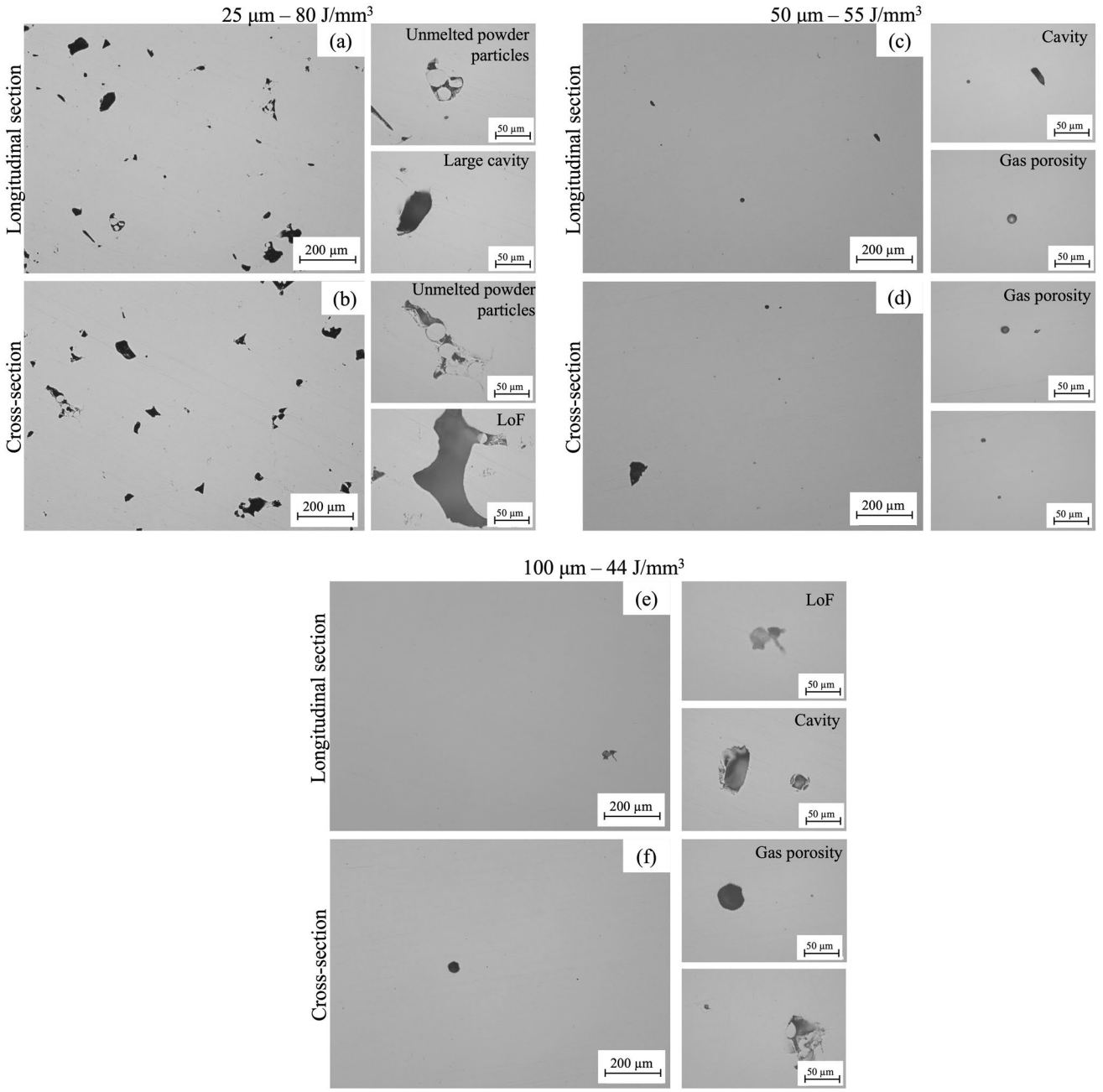

Figure 4 Representative OM micrographs showing some defects detected in longitudinal section (**a**, **c**, **e**) and cross section (**b**, **d**, **f**) of the cubic samples fabricated according to the different layer thicknesses and corresponding LED values. For each layer thickness and LED value, the subsize micrographs on the right show the same defects visible on the micrographs on the left, but at higher magnification.

local cooling rates and thermal conductivity that are strongly dependent on the mass of the molten pool. It should be mentioned that this evidence was already mentioned in [37, 69]. The microstructure of the samples fabricated with a 25 µm layer thickness exhibits high number of defects including LoF, unmelted powder particles and small cavities located at the triple intersection of the melt pools (Fig. 6a, d), known to be susceptible to thermal instability and incomplete fusion due to overlapping melt tracks. These defects are notably reduced in samples fabricated with 50 µm layer thickness (Fig. 6b, e), likely due to the improved

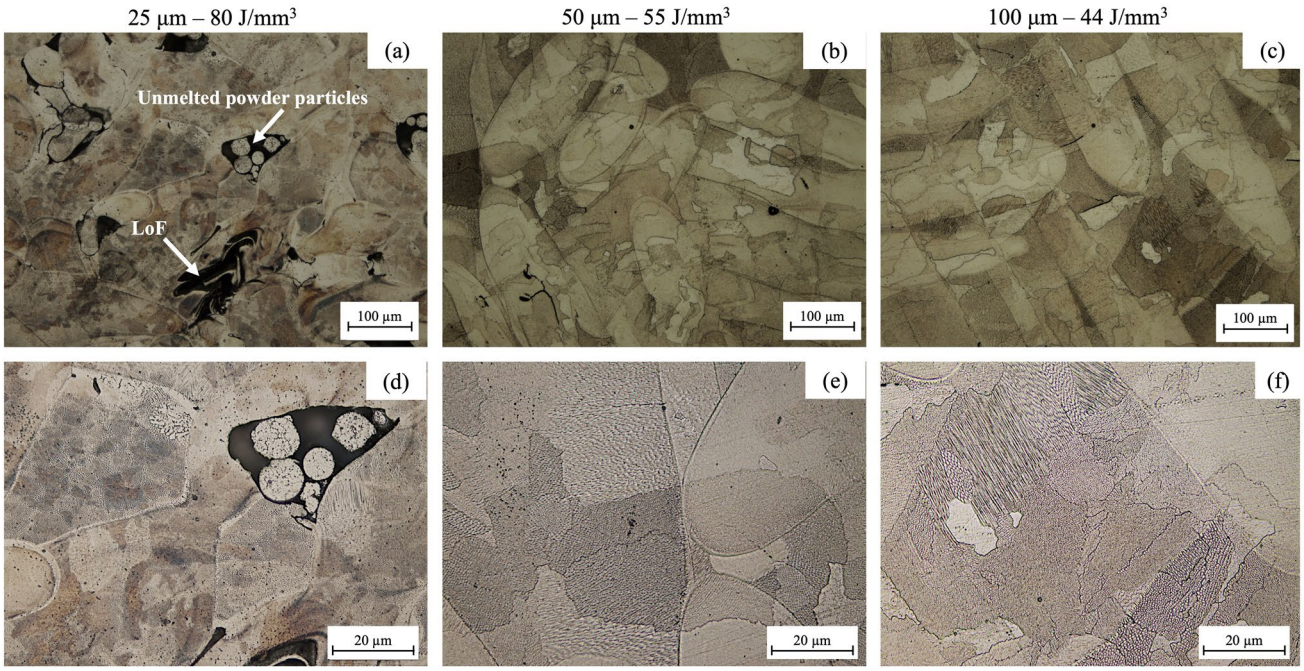

Figure 5 Representative OM micrographs of the microstructure in cross section of the cubic samples fabricated according to the different layer thicknesses and corresponding LED values: **a**, **d** 25 µm–80 J/mm^3; **b**, **e** 50 µm–55 J/mm^3; **c**, **f** 100 µm–44 J/mm^3.

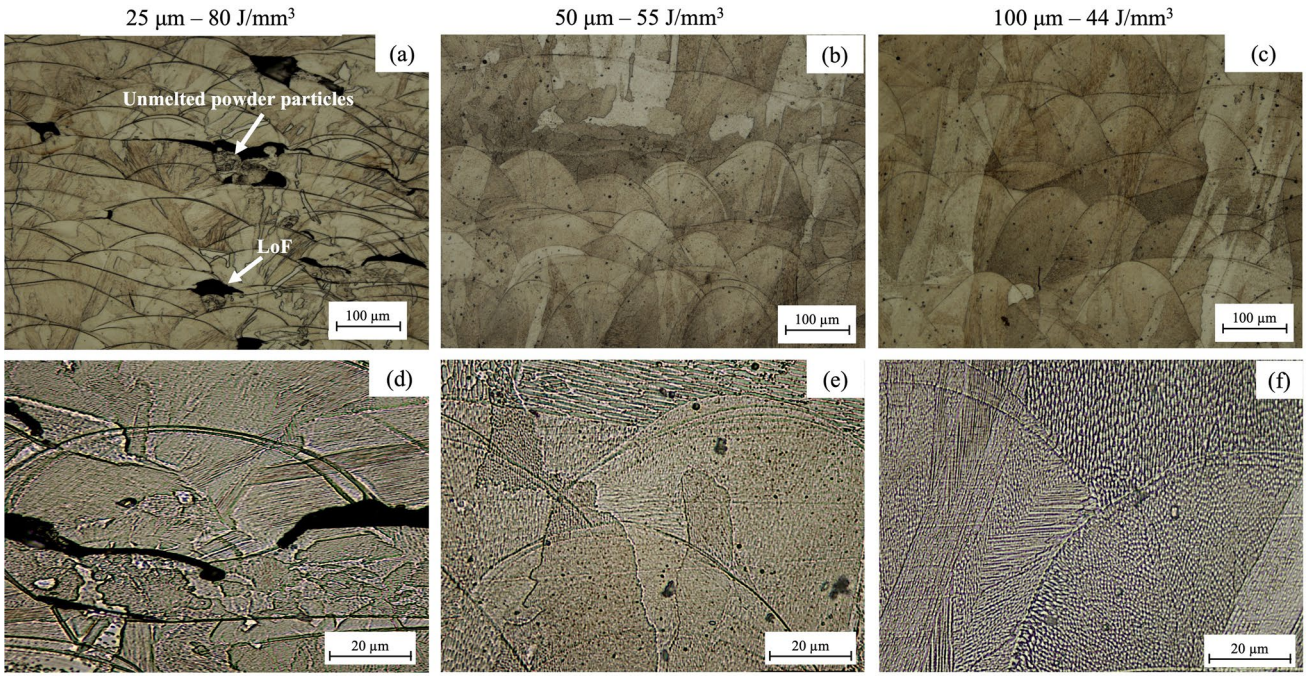

Figure 6 Representative OM micrographs of the microstructure in longitudinal section of the cubic samples fabricated according to the different layer thicknesses and corresponding LED values: **a**, **d** 25 µm–80 J/mm^3; **b**, **e** 50 µm–55 J/mm^3; **c**, **f** 100 µm–44 J/mm^3.

thermal balance and more effective melt pool overlap. Such evidence is consistent with a previous work by Kale et al. [47].

The grain and sub-grain microstructures in Fig. 6 were further investigated by SEM. Irrespective of the selected process parameters, the representative

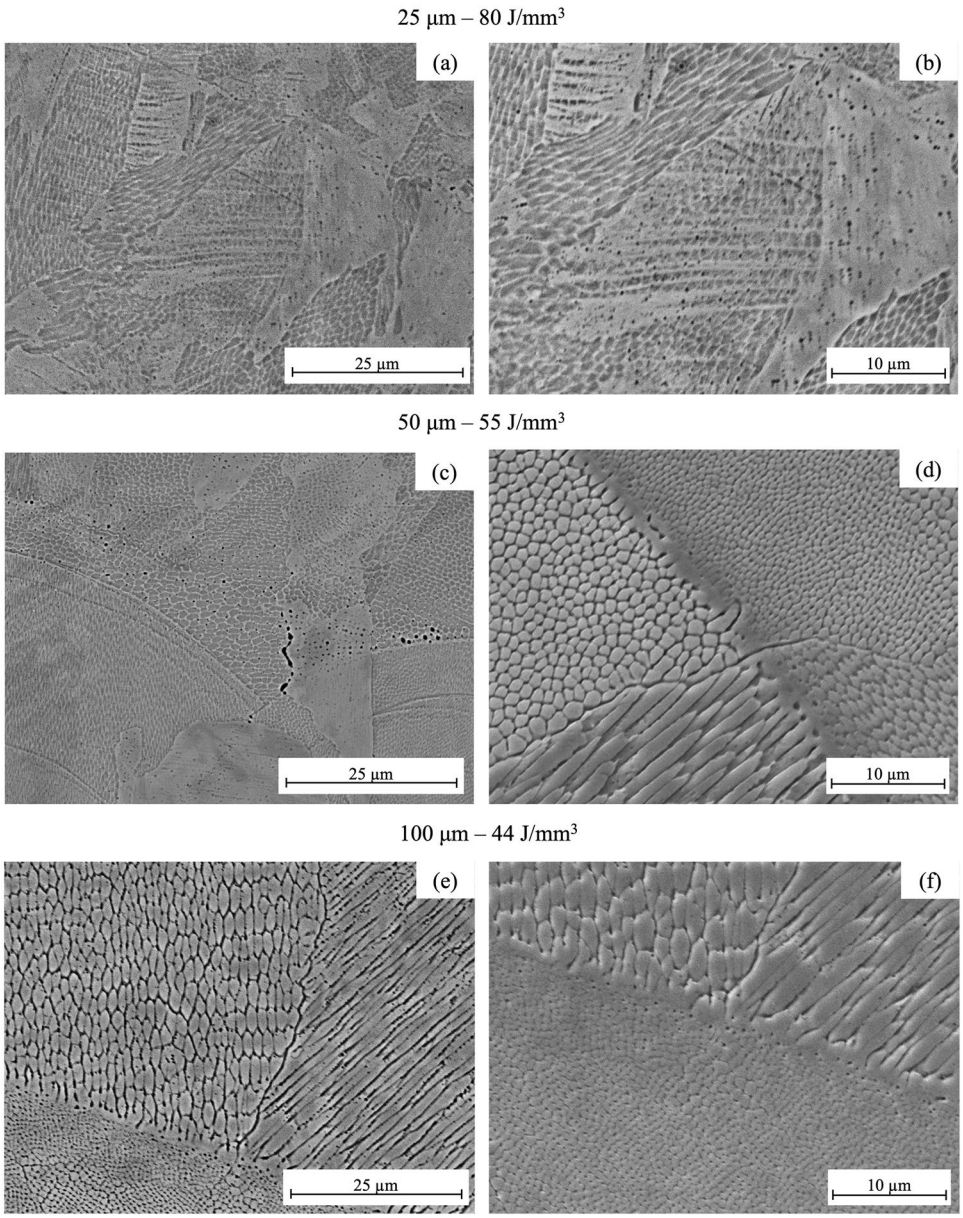

Figure 7 Representative SEI-SEM micrographs of the microstructure in cross section of the cubic samples fabricated according to the different layer thicknesses and corresponding LED values: **a**, **b** 25 µm–80 J/mm^3; **c**, **d** 50 µm–55 J/mm^3; **e**, **f** 100 µm–44 J/mm^3.

SEI-SEM micrographs in Fig. 7 that show the cross-sectional microstructure of cubic samples, highlight the typical microstructural features of metallic materials fabricated by the L-PBF process. As shown in Fig. 7a, b the growth direction of the columnar grains within the melt pools aligns with the thermal gradient and a fine cellular dendritic microstructure is also detectable within grains. This cellular structure arises from the reduced constitutional undercooling generated by the high L-PBF thermal gradient and from the solute segregation inherent to the process. Both layer thickness and localized thermal gradients affect the size and morphology of the dendritic cells, as well as their local direction of growth within the melt pool itself. In samples fabricated with 50 µm layer thickness (Fig. 7c, d) grain growth and cellular dendritic structure similar to those observed for the material processed with a layer thickness of 25 µm were found. However, an increase in size of the cellular dendritic structure with the layer thickness was noted (i.e., passing from 25 to 50 µm), thus corroborating the OM results and the experimental findings previously reported in [63, 70]. Regardless of the layer thickness, cells near the melt pool boundaries are smaller and more equiaxed than at the center of the pool, due to the radial heat flow and rapid solidification at pool edges. For samples printed at 50 µm

and 100 µm layer thicknesses (Fig. 7e, f), no notable changes in orientation and size of the microstructure were observed. Hence, a coarser microstructure was generally associated with high layer thickness and low LED values, underscoring the critical role of the cooling rate in the development of the microstructure. At last, SEM analyses further confirmed the presence of many LoF defects. As an example, some unmelted powder particles in the microstructure of the cubic samples fabricated with the 25 µm layer thickness are depicted in Fig. 8. Overall, the microstructural characterization using optical microscopy and scanning electron microscopy suggests that layer thicknesses of 50 µm and 100 µm are prone to increase the material properties mainly due to a small number of defects.

Mechanical properties

The tensile properties of the samples fabricated with different building directions and layer thicknesses are summarized in Table 3. Moreover, for each layer thickness, the average stress–strain curves for samples built according to the *xy* (horizontal) and *xz* (vertical) directions are shown in Figs. 9 and 10, respectively. According to the above-mentioned parameters, some differences in the tensile properties of the steel examined could be detected. The Young's Modulus (E) displays higher mean values in the *xy* direction compared to the *xz* one, probably due to a better stiffness of the inter-layer material when subjected to tensile stresses perpendicular to the elongated grains rather than parallel to them. Concerning the ultimate tensile strength (UTS), it reaches the maximum (656 ± 3 MPa) (Table 3) for the combination of *xy* building direction and 50 µm layer thickness. Meanwhile, samples with the lowest layer thickness (25 µm) exhibited the lowest UTS for both building directions. The observed differences between *xy* and *xz* building directions quantify the mechanical anisotropy of L-PBF AISI 316L. Specifically, the anisotropy ratio for UTS ranges from 1.12 to 1.16, depending on layer thickness, indicating moderate anisotropy that slightly decreases with increasing layer thickness. This behavior stems from the columnar grain structure oriented predominantly along the building direction, which provides greater resistance to deformation when loading is perpendicular to the grain orientation. This trend is driven by the microstructural behavior occurred due to the high energy density supplied and that is necessary to melt

Table 3 Summary of the tensile properties of the samples fabricated according to the different building directions and layer thicknesses

Sample	Young modulus [GPa]	Yield strength [MPa]	Ultimate tensile strength [MPa]	Elongation at fracture [%]
25 µm-xy	157 ± 6	488 ± 2	608 ± 2	28 ± 1
50 µm-xy	168 ± 1	516 ± 3	656 ± 3	30 ± 1
100 µm-xy	173 ± 4	503 ± 2	644 ± 2	30 ± 2
25 µm-xz	92 ± 5	470 ± 1	524 ± 13	21 ± 12
50 µm-xz	92 ± 4	470 ± 4	573 ± 4	34 ± 1
100 µm-xz	102 ± 2	457 ± 4	572 ± 4	30 ± 3

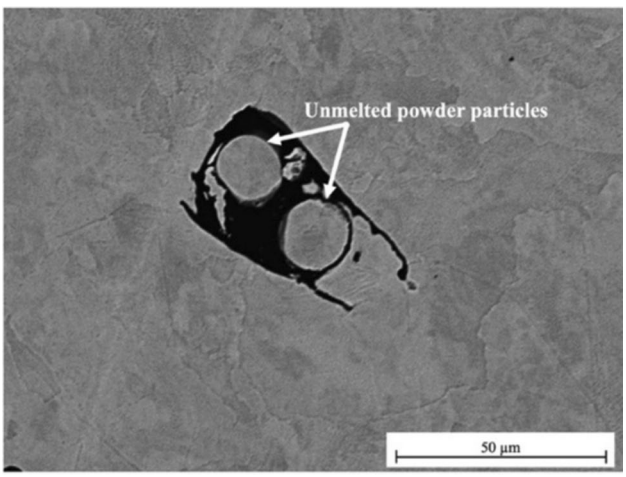

Figure 8 SEI-SEM micrograph of unmelted powder metallic particles in the microstructure of the cubic samples fabricated with the 25 µm layer thickness.

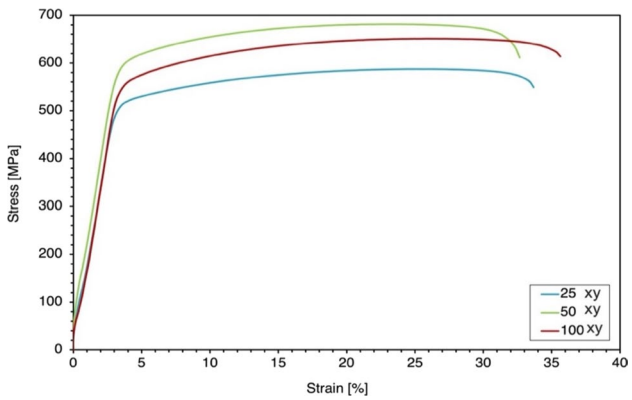

Figure 9 Average stress–strain curves for samples built according to the *xy* (horizontal) direction and the different layer thicknesses.

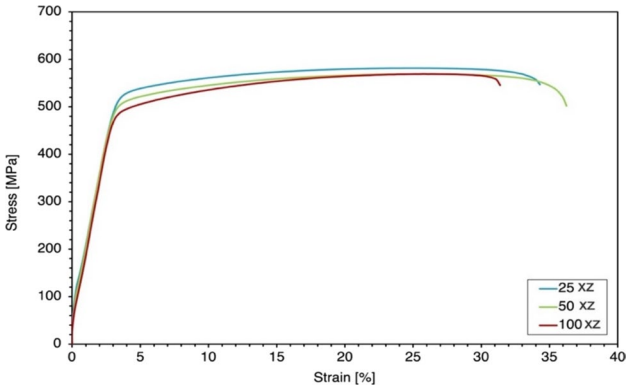

Figure 10 Average stress–strain curves for samples built according to the *xz* (vertical) direction and the different layer thicknesses.

the material during the laser scan. With layer thickness of 25 μm, smaller and more equiaxed grains are observed on the melt pool boundaries (Fig. 7a, b) and elongated at the center of the pool (Fig. 7d). For samples printed at 50 μm and 100 μm layer thicknesses only a slightly change in the core size is noted, being reduced predominantly due to the role of the direction of cooling rate. Presumably, this occurs due to the material volume within the melt pool. Samples printed at 25 μm layer thickness show a narrow depth of the melt pool with a low amount of material to remelt. Thus, most of the melt pool is surrounded by solid metallic material with high thermal conductivity providing very fast heat dissipation, leading to intensified evaporation and increasing the possibility to defect formation. Parallelly, with 50 and 100 μm layer thicknesses, the remelted quantity of material of the previous layer reduces, which means a larger volume of the melt pool, which is surrounded by the powder. Thus there is less significant heat dissipation, enhancing the correct material solidification. This is also found on different research works [37, 71–73]. This may be correlated with the high quantity of defects detected by OM and SEM, which affect the material's behavior during testing. These defects act as stress concentrators and reduce the material's ability to withstand tensile loading, as also noted in prior research [74]. In addition, the yield strength (YS) increases depending on the building direction. The influence of building direction and layer thickness on the mechanical resistance of the L-PBF AISI 316L is better displayed in the comparative plots of Fig. 11. As can be seen, the UTS and YS are mainly affected by the building direction that, with a preferential orientation of grains in the solidification mechanism in the *xy* direction, has a reduced isotropic effect in mechanical properties. The UTS and YS are also affected, to a minor extent, by the layer thickness. In fact, data demonstrate that the mechanical resistance of the samples is more sensitive to the build orientation than to the layer thickness. However, the combination of 50 μm layer thickness and *xy* direction yielded the best mechanical performance. These results reinforce the importance of optimizing process parameters for improving the density and the microstructural features, such as the reduction of defects and the optimization of the cellular dendritic structure, thus achieving the desired mechanical properties in functional parts.

Impact strength tests were then performed on V-notched samples at room temperature by using an instrumented Charpy pendulum. This approach enabled the acquisition of the load–displacement curve, thus allowing a more in-depth analysis of the fracture mechanics by separating the complementary energy contributions during crack initiation and propagation. For each layer thickness, the average load–displacement curves for samples built according to the *xy* and *xz* building directions are reported in Fig. 12. The average load–displacement curves exhibit slight differences with layer thickness, which become more pronounced as the thickness increases from 50 to 100 μm. Moreover, a noticeable effect of the building direction was detected only for samples fabricated with a 50 μm layer thickness, which exhibited higher impact resistance when printed in the *xz* direction. The impact test results are also illustrated in the bar chart in Fig. 13 showing the mean total absorbed energy for samples in each building direction and layer thickness condition prior to fracture. Regardless of the building direction, the total absorbed energy of the samples printed at 25 μm layer thickness is the lowest, reaching mean values of about 28 J; accordingly, these samples show the worst impact behavior of the whole experimental campaign. This inferior performance is consistent with the higher density of microstructural defects previously observed via OM and SEM, which act as stress concentrators and, thus reducing both initiation resistance and crack growth stability. Conversely, samples printed at 50 μm and 100 μm layer thicknesses were the toughest, demonstrating high impact resistance and reaching mean values of the total absorbed energy of about 121 J. These values are consistent with those previously reported in the literature for AM samples

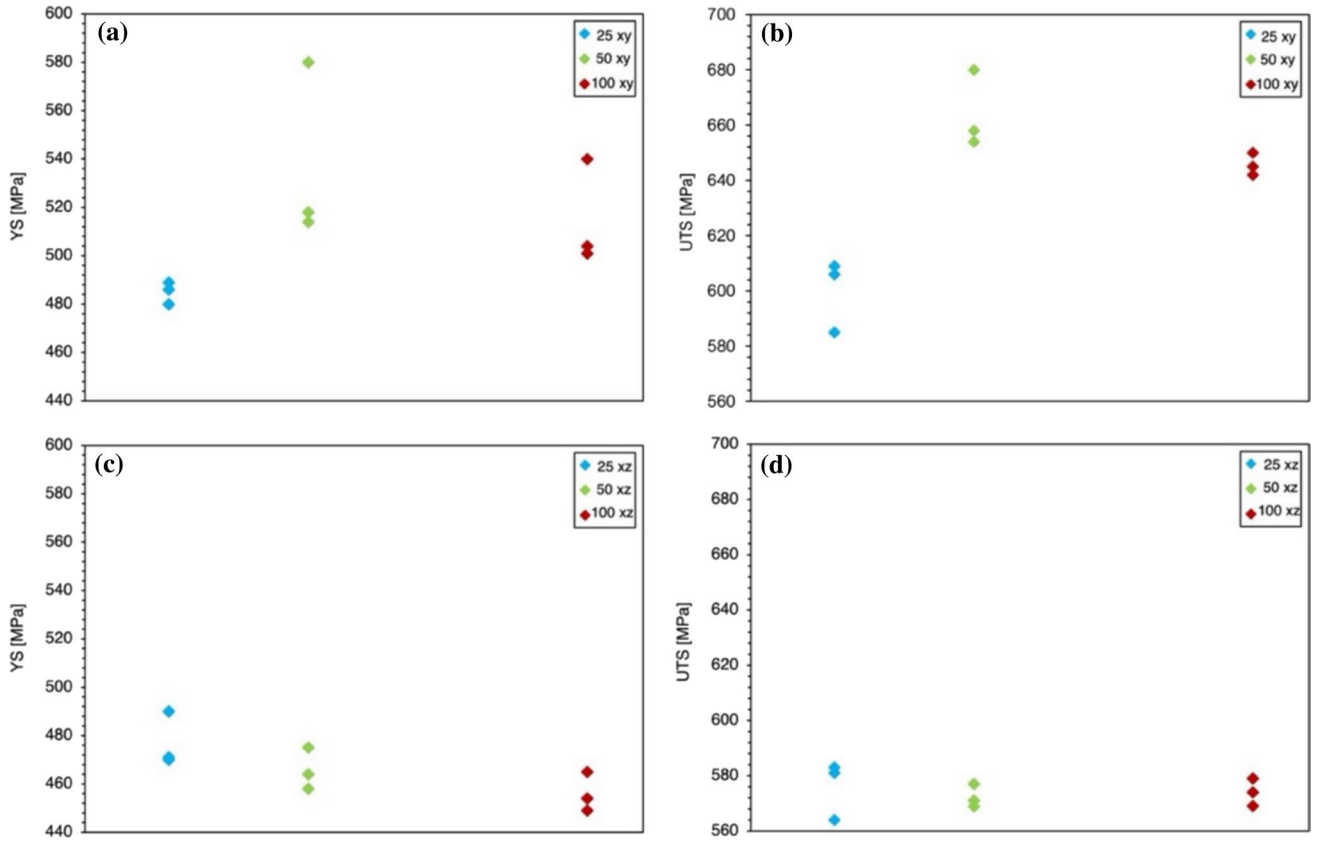

Figure 11 Comparative plots of the tensile properties of the samples fabricated according to the different building directions and layer thicknesses: **a**, **b** YS and UTS in *xy* direction and in all layer thickness conditions, respectively; **c**, **d** YS and UTS in *xz* direction and in all layer thickness conditions, respectively.

tested at room temperature, in which high levels of gas porosity, cracking and other defects limited the impact energies to approximately 15–70 J [18, 45]. Reducing these defects could improve the absorbed energy, resulting in impact toughness within a range of 130–165 J [42, 43, 45, 75–77]. The present samples exhibited an increase in the mean apparent density with increasing the layer thickness. Hence, not only the presence of defects but also the selected layer thickness has a strong effect on the toughness behavior regardless of the building direction, as also highlighted in [45, 78, 79]. Figure 14 shows the complementary contributions of initiation energy (corresponding to the area below the force–displacement curve up to the peak force point) and propagation energy (corresponding to the area below the force–displacement curve from the peak force point and beyond), registered during the impact tests of the samples fabricated according to the considered building directions and layer thicknesses. There is a clear dependence on layer thickness; samples printed in both building directions and at 25 μm layer thickness show low initiation energy and reduced impact strength before rupture, leading to an imminent yielding of the specimens. Therefore, their propagation energy is high. Conversely, samples printed at 50 μm and 100 μm layer thicknesses displayed a nearly equal contribution between initiation and propagation energies, demonstrating superior overall toughness. Even though for similar combinations of layer thicknesses and building directions the total absorbed energies are of the same order of magnitude as data published in [18, 43, 45, 75, 76, 78–80], in this paper the use of an instrumented Charpy testing allowed to reveal that the layer thickness plays a critical role in initiation and propagation energies, showing that 50 μm of layer thickness is the optimal for improving the impact toughness.

At first, the SEM analyses were performed on the fracture surfaces of tensile specimens printed in *xy* direction (Fig. 15) to identify the main failure

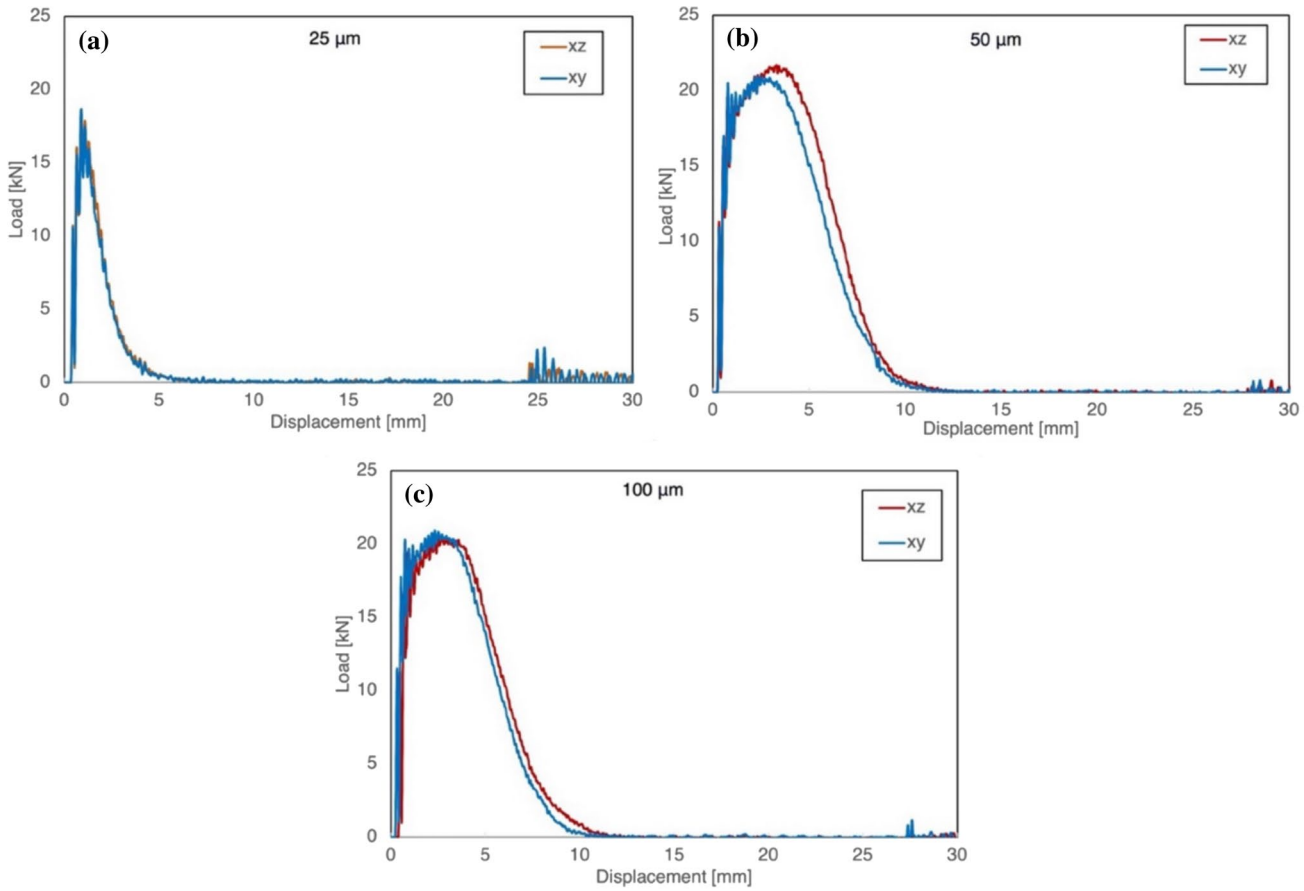

Figure 12 Average load–displacement curves of the samples fabricated according to the different building directions and: **a** 25 µm layer thickness; **b** 50 µm layer thickness; **c** 100 µm layer thickness.

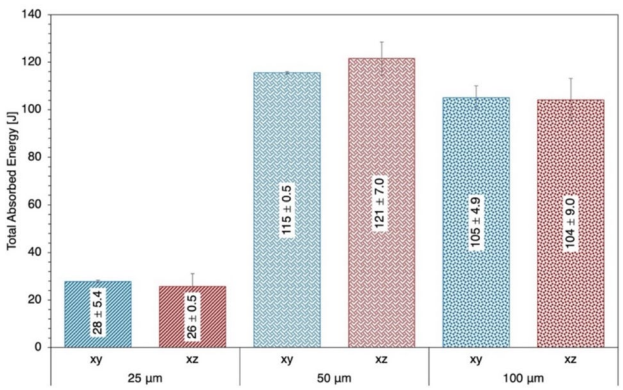

Figure 13 Bar chart of the mean total absorbed energy acquired during impact tests for the samples fabricated according to the different building directions and layer thicknesses.

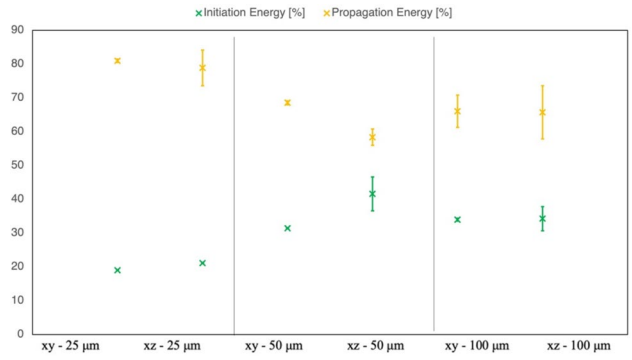

Figure 14 Complementary contribution of initiation and propagation energies registered during the impact tests of the samples fabricated according to the different building directions and layer thicknesses.

mechanisms associated with the different layer thicknesses. At the microscopic scale, these specimens predominantly exhibited a ductile fracture mechanism, characterized by the presence of a great number of dimples and microvoids, as pointed out by the white arrows in Fig. 15a, c. The samples with a

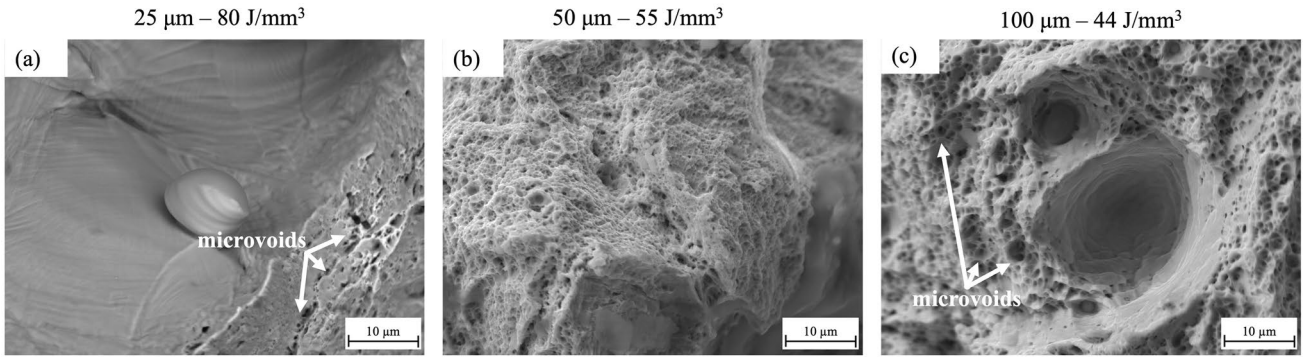

Figure 15 Representative SEI-SEM micrographs of the fracture surface of tensile samples built in *xy* direction and according to: **a** 25 µm layer thickness; **b** 50 µm layer thickness; **c** 100 µm layer thickness.

layer thickness of 50 µm (Fig. 15b) exhibit fewer and smaller features compared to those printed with a layer thickness of 25 µm (Fig. 15a). In these samples, local areas characterized by a brittle fracture mechanism can also be detected, mainly located near the microstructural defects previously identified acting as stress concentrator. These defects acted as crack initiation sites, contribute to mixed-mode fracture behavior and resulting in the lowest mechanical performance of the samples fabricated with a layer thickness of 25 µm. Conversely, samples fabricated with 50 µm of layer thickness exhibited more uniform and refined dimple's morphology as well as, with fewer brittle zones than those produced with a layer thickness of 25 µm. This is evidence of a predominant ductile failure mechanism, correlated with improved mechanical properties discussed in previous sections. The specimens printed with a layer thickness of 100 µm revealed a surface step formation on a ductile fracture dimple wall (Fig. 15c), which are typically associated with the interaction of dislocation slip bands across plastically deformed regions. This behavior is usually observed on very ductile materials due to the interaction of a dislocation slip band across the dimple walls, reflecting enhanced plastic fracture mechanisms and supporting the relatively high toughness. These findings are consistent with previous data reported in [81, 82]. The fractographic evidence confirms that ductile mechanism is the dominant fracture mode across all processing conditions, but the layer thickness notably influences the size, morphology and distribution of ductile features, as well as the presence of brittle zones. However, a layer thickness of 50 µm appears to be the best process condition, as it minimizes microstructural defects and promotes uniform plastic deformation at failure.

Figure 16a–c depicts the macrographs of the fracture surfaces of Charpy impact specimens built in *xy* direction and according to the different layer thicknesses. The red dashed lines in the same images qualitatively enclose the regions of the samples defined as the unstable fracture regions according to the ASTM E23 standard [83]. For completeness, the scheme in Fig. 16d reports the different regions of a typical fracture surface of a broken V-notched Charpy sample. According to the abovementioned standard, the V-notch fracture surface can be divided into four regions: the unstable fracture region, the fracture initiation region, the shear lips region, and the final fracture region. The latter three regions can also be merged and considered as a unique "shear area," which is responsible for the most total absorbed energy during impact testing. As evident from the macrographs, the morphology of the V-notched fracture surfaces changes markedly with layer thickness. The samples fabricated with 50 µm and 100 µm layer thicknesses (Fig. 16b, c, respectively) exhibit the greatest lateral expansions, indicative of enhanced plastic deformation and higher impact toughness. This agrees with the higher total absorbed energy values of these specimens compared to those absorbed by the samples printed with a 25 µm layer thickness.

Representative SEI-SEM micrographs of the fracture surface near the crack initiation area of Charpy impact specimens built along the *xy* direction and with different layer thicknesses are depicted in Fig. 17. Once again, samples printed with a 25 µm layer thickness

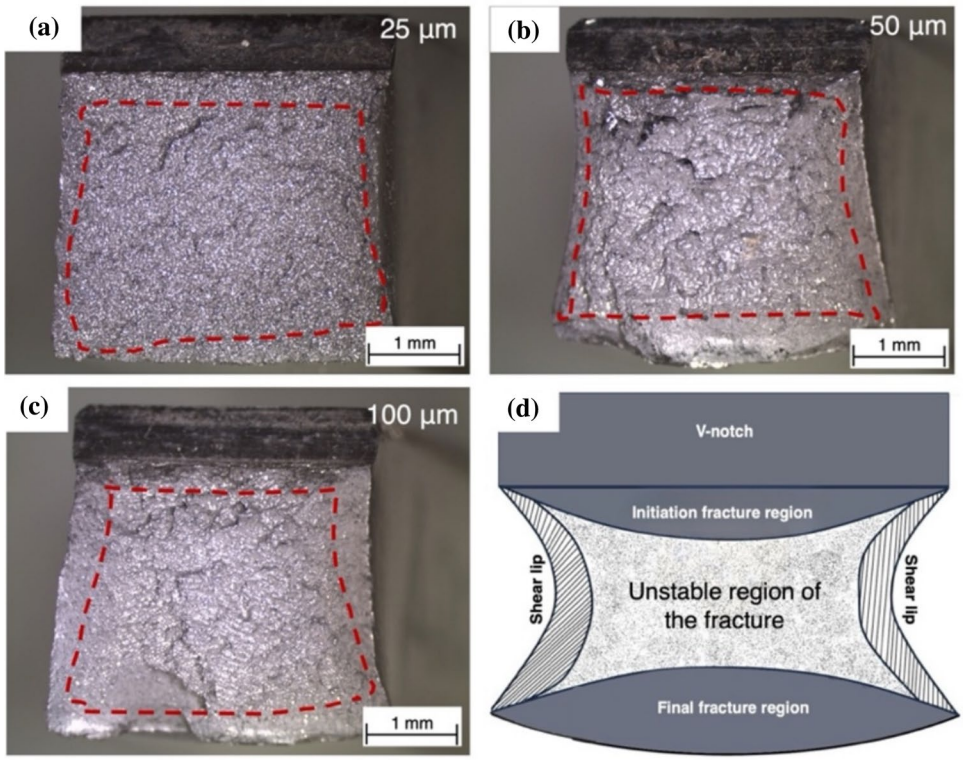

Figure 16 Macrographs of the fracture surfaces of Charpy impact specimens built in *xy* direction and according to: **a** 25 µm layer thickness; **b** 50 µm layer thickness; **c** 100 µm layer thickness. The red dashed lines in (**a–c**) qualitatively enclose the regions of the samples defined as the unstable fracture regions according to the ASTM E23 standard. Scheme in **d** represents the different regions of a typical fracture surface of a broken V-notched Charpy sample.

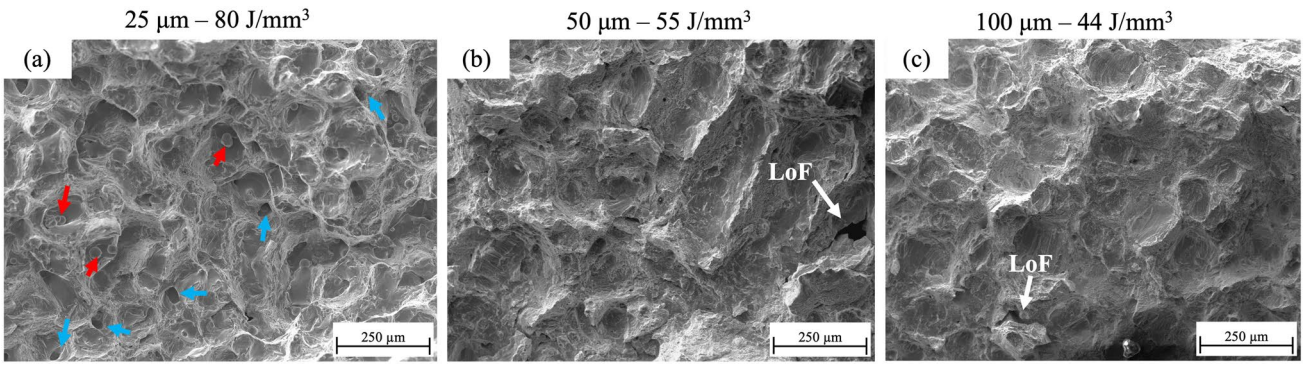

Figure 17 Representative SEI-SEM micrographs of the fracture surface near the initiation area of Charpy impact specimens built in *xy* direction and according to: **a** 25 µm layer thickness; **b** 50 µm layer thickness; **c** 100 µm layer thickness. (Red arrows: unmelted powder particles; blue arrows: voids due to microporosity; white arrows: LoF defects).

show a less ductile fracture compared to those printed with 50 and 100 µm layer thicknesses.

In Fig. 17a, the presence of unmelted powder particles (red arrows) as well as voids due to microporosity (blue arrows) can be identified. None of these defects were found in the fracture surfaces of the specimens printed with 50 and 100 µm of layer thicknesses, although in these samples the occasional presence of LoF defects was detected (white arrows in Fig. 17b, c). It is worth noting that the presence of pores and unmelted powder particles strongly influenced the fracture path of the Charpy impact samples and thus their fracture toughness, acting as stress concentrators and reducing the energy required to initiate and propagate cracks. These findings highlight the importance of layer thickness optimization in controlling fracture mechanisms and improving impact toughness performance.

Conclusions

In this study, density, tensile and Charpy impact specimens in AISI 316L steel were produced via L-PBF with three different sets of process parameters. Particularly, three different layer thicknesses and thus different sets of LED values were selected to allow the fabrication of samples according to both horizontal and vertical directions with respect to the building platform. Based on the experimental results, the following conclusions can be drawn:

- The mean apparent density was consistent with the presence of gas porosity and LoF defects and strongly related to the variation in the layer thickness. The lowest mean apparent density was detected in samples fabricated with a 25 μm layer thickness, probably due to the highest content of internal defects.
- A slight increase in the size of the cellular dendritic structure of grains within the melt pools was observed with increasing layer thickness from 25 to 50 μm.
- The best compromise between defect content and coarseness of the microstructure was detected in samples fabricated with a 50 μm of layer thickness.
- The tensile and impact strength properties showed a slight dependence on the building direction. Samples fabricated with a 25 μm layer thickness gained the lowest mechanical properties, whereas those printed at 50 μm layer thickness was demonstrated to be the best choice for achieving the maximum tensile strength and the highest total absorbed energy during Charpy impact testing.
- Samples printed with a 25 μm layer thickness exhibited a less ductile fracture than those printed at 50 and 100 μm layer thicknesses. The morphology of the fracture surfaces of Charpy impact specimens showed that unmelted powder particles strongly influenced the fracture path during crack propagation, thus emphasizing the importance of an optimization of the process parameters for enhancing the mechanical performance of L-PBF AISI 316L steel.

Acknowledgements

The authors wish to acknowledge Eng. Davide Di Curzio and Eng. Paolo Morelli of ANSA TECH srl (Finale Emilia, Modena, Italy) for providing the samples analyzed in the present research. The authors also acknowledge Eng. Riccardo Osti and Eng. Dario Pezzini for their support in the experimental analysis.

Author contributions

M. Merlin, A. Fortini C. Soffritti and C. Morales were involved in conceptualization; M. Merlin, A. Fortini and C. Morales contributed to methodology; C. Morales, M. Actis Grande, M. Merlin, A. Fortini, M. Gragnanini and C. Soffritti were involved in formal analysis and investigation; C. Morales and M. Merlin contributed to writing—original draft preparation; C. Morales and M. Actis Grande, M. Merlin, A. Fortini, M. Gragnanini and C. Soffritti were involved in writing—review and editing. M. Merlin and A. Fortini contributed in funding acquisition; M. Merlin and A. Fortini were involved in resources; M. Merlin and A. Fortini were involved in supervision.

Funding

Open access funding provided by Università degli Studi di Ferrara within the CRUI-CARE Agreement. This research work was financially supported by the FAR 2024 of the University of Ferrara (Grant Number 2024-FAR.L_DE_MM).

Data availability

The raw data required to reproduce these findings are available from the corresponding author of this paper. The processed data required to reproduce these findings are available from the corresponding author of this paper.

Declarations

Conflict of interest The authors declare that no known competing financial interests or personal relationships that could have appeared to influence the work reported in this paper.

Ethical approval The manuscript is original and is not being submitted for publication elsewhere.

Consent for publication All authors approve the manuscript for publication.

References

[1] Gibson I, Rosen D, Stucker B (2015) Additive manufacturing technologies: 3D printing, rapid prototyping, and direct digital manufacturing, 2nd edn. Springer, New York ISBN 9781493921133

[2] Singh R, Gupta A, Tripathi O, Srivastava S, Singh B, Awasthi A, Rajput SK, Sonia P, Singhal P, Saxena KK (2019) Powder bed fusion process in additive manufacturing: an overview. Mater Today Proc 26:3058–3070. https://doi.org/10.1016/j.matpr.2020.02.635

[3] Yadroitsev I, Yadroitsava I, Du Plessis A, MacDonald E (2021) Fundamentals of laser powder bed fusion of metals, 1st edn. Elsevier ISBN 978-0-12-824090-8

[4] Dufera S, Srinivasulu Reddy K (2016) Additive manufacturing technologies. Int J Manag Inf Technol Eng 4(7):89–112

[5] Liverani E, Toschi S, Ceschini L, Fortunato A (2017) Effect of selective laser melting (SLM) process parameters on microstructure and mechanical properties of 316L austenitic stainless steel. J Mater Process Technol 249:255–263. https://doi.org/10.1016/j.jmatprotec.2017.05.042

[6] Zhu Z, Hu Z, Seet HL, Liu T, Liao W, Ramamurty U, Ling Nai SM (2023) Recent progress on the additive manufacturing of aluminum alloys and aluminum matrix composites: microstructure, properties, and applications. Int J Mach Tools Manuf. https://doi.org/10.1016/j.ijmachtools.2023.104047

[7] Tan Q, Zhang M (2024) Recent advances in inoculation treatment for powder-based additive manufacturing of aluminium alloys. Mater Sci Eng R Rep. https://doi.org/10.1016/j.mser.2024.100773

[8] Kotadia HR, Gibbons G, Das A, Howes PD (2021) A review of laser powder bed fusion additive manufacturing of aluminium alloys: microstructure and properties. Addit Manuf. https://doi.org/10.1016/j.addma.2021.102155

[9] Bajaj P, Hariharan A, Kini A, Kürnsteiner P, Raabe D, Jägle EA (2020) Steels in additive manufacturing: a review of their microstructure and properties. Mater Sci Eng A. https://doi.org/10.1016/j.msea.2019.138633

[10] Joseph AS (2024) Laser powder bed fusion of steels: processing, mechanical properties, microstructure, defects, control methods and current challenges: a review. J Adv Eng Res 11:135–144

[11] Narasimharaju SR, Zeng W, See TL, Zhu Z, Scott P, Jiang X, Lou S (2022) A comprehensive review on laser powder bed fusion of steels: processing, microstructure, defects and control methods, mechanical properties, current challenges and future trends. J Manuf Process 75:375–414. https://doi.org/10.1016/j.jmapro.2021.12.033

[12] Haase F, Siemers C, Rösler J (2023) Laser powder bed fusion (LPBF) of commercially pure titanium and alloy development for the LPBF process. Front Bioeng Biotechnol. https://doi.org/10.3389/fbioe.2023.1260925

[13] Cao S, Zou Y, Lim CVS, Wu X (2021) Review of laser powder bed fusion (LPBF) fabricated Ti-6Al-4V: process, post-process treatment, microstructure, and property. Light: Adv Manuf. https://doi.org/10.37188/lam.2021.020

[14] Mahmood MA, Ur Rehman A, Ristoscu C, Demir M, Popescu-Pelin G, Pitir F, Salamci MU, Mihailescu IN (2022) Advances in laser additive manufacturing of cobalt–chromium alloy multi-layer mesoscopic analytical modelling with experimental correlations: from micro-dendrite grains to bulk objects. Nanomaterials. https://doi.org/10.3390/nano12050802

[15] Li K, Yang T, Gong N, Wu J, Wu X, Zhang DZ, Murr LE (2023) Additive manufacturing of ultra-high strength steels: a review. J Alloys Compd. https://doi.org/10.1016/j.jallcom.2023.171390

[16] Sohrabi N, Ran R, Duro PA, Cayron C, Jhabvala J, Pejchal V, Sereda O, Logé RE (2023) Laser powder-bed fusion of a high entropy alloy with outstanding intrinsic mechanical properties. J Alloys Compd. https://doi.org/10.1016/j.jallcom.2023.169209

[17] Istituto Italiano della Saldatura metal additive manufacturing e powder bed fusion: Principi Di Progettazione Corso Pilota per metal additive manufacturing design: Panoramica Sulle Caratteristiche Generali (2017)

[18] Tolosa I, Garciandía F, Zubiri F, Zapirain F, Esnaola A (2010) Study of mechanical properties of AISI 316 stainless steel processed by "selective laser melting", following different manufacturing strategies. Int J Adv Manuf Technol 51:639–647. https://doi.org/10.1007/s00170-010-2631-5

[19] Lodhi MJK, Deen KM, Greenlee-Wacker MC, Haider W (2019) Additively manufactured 316L stainless steel with improved corrosion resistance and biological response for biomedical applications. Addit Manuf 27:8–19. https://doi.org/10.1016/j.addma.2019.02.005

[20] Fang K, Luo K, Wang L (2022) Effect of microstructure on mechanical properties of 316 LN austenitic stainless steel. Coatings. https://doi.org/10.3390/coatings12101461

[21] Svahn F, Mishra P, Edin E, Åkerfeldt P, Antti ML (2024) Microstructure and mechanical properties of a modified 316 austenitic stainless steel alloy manufactured by laser powder bed fusion. J Mater Res Technol 28:1452–1462. https://doi.org/10.1016/j.jmrt.2023.12.063

[22] Abdulaziz B (2017) Additive manufacturing of high performance 316L stainless steel nano composites via SLM

[23] Abu-warda N, Bedmar J, García-Rodriguez S, Torres B, Utrilla MV, Rams J (2024) Effect of post-processing heat treatments on the high-temperature oxidation of additively manufactured 316L stainless steel. J Mater Res Technol 29:3465–3476. https://doi.org/10.1016/j.jmrt.2024.01.270

[24] Saboori A, Aversa A, Marchese G, Biamino S, Lombardi M, Fino P (2020) Microstructure and mechanical properties of AISI 316L produced by directed energy deposition-based additive manufacturing: a review. Appl Sci. https://doi.org/10.3390/app10093310

[25] Evangelou A, Stylianou R, Loizou A, Kim D, Liang A, Reed P, Constantinides G, Kyratsi T (2023) Effects of process parameters and scan strategy on the microstructure and density of stainless steel 316 L produced via laser powder bed fusion. J Alloys Metall Syst 3:1–13. https://doi.org/10.1016/j.jalmes.2023.100027

[26] Gor M, Soni H, Wankhede V, Sahlot P, Grzelak K, Szachgluchowicz I, Kluczyński J (2021) A critical review on effect of process parameters on mechanical and microstructural properties of powder-bed fusion additive manufacturing of SS316L. Materials 14(21):6527. https://doi.org/10.3390/ma14216527

[27] Hahne W (2021) Optimization of laser powder bed fusion process parameters for 316L stainless steel. Master's Thesis (University of Uppsala, Uppsala)

[28] Pragana JPM, Pombinha P, Duarte VR, Rodrigues TA, Oliveira JP, Bragança IMF, Santos TG, Miranda RM, Coutinho L, Silva CMA (2020) Influence of processing parameters on the density of 316L stainless steel parts manufactured through laser powder bed fusion. Proc Inst Mech Eng Part B: J Eng Manuf 234:1246–1257. https://doi.org/10.1177/0954405420911768

[29] Fayazfar H, Salarian M, Rogalsky A, Sarker D, Russo P, Paserin V, Toyserkani EA (2018) Critical review of powder-based additive manufacturing of ferrous alloys: process parameters, microstructure and mechanical properties. Mater Des 144:98–128. https://doi.org/10.1016/j.matdes.2018.02.018

[30] Ma M, Wang Z, Gao M, Zeng X (2015) Layer thickness dependence of performance in high-power selective laser melting of 1Cr18Ni9Ti stainless steel. J Mater Process Technol 215:142–150. https://doi.org/10.1016/j.jmatprotec.2014.07.034

[31] Peng T, Chen C (2018) Influence of energy density on energy demand and porosity of 316L stainless steel fabricated by selective laser melting. Int J Precis Eng Manuf-Green Technol 5:55–62. https://doi.org/10.1007/s40684-018-0006-9

[32] Choi JP, Shin GH, Brochu M, Kim YJ, Yang SS, Kim KT, Yang DY, Lee CW, Yu JH (2016) Densification behavior of 316L stainless steel parts fabricated by selective laser melting by variation in laser energy density. Mater Trans 57:1952–1959. https://doi.org/10.2320/matertrans.M2016284

[33] Lee HJ (2022) Effects of the energy density on pores, hardness, surface roughness, and tensile characteristics of deposited ASTM 316L specimens with powder-bed fusion process. Materials. https://doi.org/10.3390/ma15196672

[34] Tucho WM, Lysne VH, Austbø H, Sjolyst-Kverneland A, Hansen V (2018) Investigation of effects of process parameters on microstructure and hardness of SLM manufactured SS316L. J Alloys Compd 740:910–925. https://doi.org/10.1016/j.jallcom.2018.01.098

[35] Spierings AB, Levy G (2009) Comparison of density of stainless steel 316L parts produced with selective laser melting using different powder grades. In: Proceedings of the SFF symposium

[36] Meier H, Haberland C (2008) Experimental studies on selective laser melting of metallic parts. Materialwiss Werksttech 39:665–670. https://doi.org/10.1002/mawe.200800327

[37] Hyer HC, Petrie CM (2022) Effect of powder layer thickness on the microstructural development of additively manufactured SS316. J Manuf Process 76:666–674. https://doi.org/10.1016/j.jmapro.2022.02.047

[38] Dabwan A, Anwar S, Al-Samhan AM, Alfaify A, Nasr MM (2021) Investigations on the effect of layers' thickness and orientations in the machining of additively manufactured stainless steel 316l. Materials. https://doi.org/10.3390/ma14071797

[39] Leicht A, Rashidi M, Klement U, Hryha E (2020) Effect of process parameters on the microstructure, tensile strength and productivity of 316L parts produced by laser powder bed fusion. Mater Charact 159:1–11. https://doi.org/10.1016/j.matchar.2019.110016

[40] Barrionuevo GO, Ramos-Grez JA, Zapata-Hidalgo D, Mullo JL, Puma-Araujo SD (2024) Influence of the processing parameters on the microstructure and mechanical properties of 316L stainless steel fabricated by laser powder bed fusion. J Manuf Mater Process 8:2–18. https://doi.org/10.3390/jmmp8010035

[41] Hamada A, Jaskari M, Gundgire T, Jarvenpaa A (2023) Enhancement and underlying fatigue mechanisms of laser powder bed fusion additive-manufactured 316L stainless steel. Mater Sci Eng A 873:1–11. https://doi.org/10.1016/j.msea.2023.145021

[42] Afkhami S, Dabiri M, Piili H, Björk T (2021) Effects of manufacturing parameters and mechanical post-processing on stainless steel 316L processed by laser powder bed fusion. Mater Sci Eng A. https://doi.org/10.1016/j.msea.2020.140660

[43] Pitrmuc Z, Šimota J, Beránek L, Mikeš P, Andronov V, Sommer J, Holešovský F (2022) Mechanical and microstructural anisotropy of laser powder bed fusion 316L stainless steel. Materials. https://doi.org/10.3390/ma15020551

[44] De Sonis E, Depinoy S, Giroux P-F, Maskrot H, Wident P, Hercher O, Villaret F, Gourgues-Lorenzon A-F (2024) Impact toughness of LPBF 316L stainless steel below room temperature. Mater Sci Eng A 915:1–16. https://doi.org/10.1016/j.msea.2024.147189

[45] Wang X, Sanchez-Mata O, Atabay SE, Muñiz-Lerma JA, Attarian Shandiz M, Brochu M (2021) Crystallographic orientation dependence of Charpy impact behaviours in stainless steel 316L fabricated by laser powder bed fusion. Addit Manuf. https://doi.org/10.1016/j.addma.2021.102104

[46] ASTM E2651-13 (2013) standard guide for powder particle size analysis. ASTM International, West Conshohocken, PA https://doi.org/10.1520/E2651-13. [Link: ASTM International, https://www.astm.org/e2651-13.html]

[47] Kale AB, Singh J, Kim BK, Kim DI, Choi SH (2020) Effect of initial microstructure on the deformation heterogeneities of 316L stainless steels fabricated by selective laser melting processing. J Mater Res Technol 9:8867–8883. https://doi.org/10.1016/j.jmrt.2020.06.015

[48] UNI EN ISO 148-1:2016 (R2023): metallic materials—Charpy pendulum impact test—part 1: test method. [Link: UNI ISO https://store.uni.com/en/uni-en-iso-148-1-2016]

[49] UNI EN ISO 14556:2023 Charpy V-notch pendulum impact test: instrumented test method. [Link: UNI ISO https://store.uni.com/en/uni-en-iso-14556-2023]

[50] ASTM E8/E8M-2 (2024) Standard test methods for tension testing of metallic materials. ASTM International, West Conshohocken, PA https://doi.org/10.1520/E0008_E0008M-24. [Link: ASTM International, https://store.astm.org/e0008_e0008m-24.html]

[51] ASTM B962-08 (2004). Standard Test methods for density of compacted or sintered powder metallurgy (PM) products using archimedes' principle. ASTM International, West Conshohocken, PA https://doi.org/10.1520/B0962-08. [Link: ASTM International, https://store.astm.org/b0962-08.html]

[52] ASTM E3-11 (2017) Standard guide for preparation of metallographic specimens. ASTM International, West Conshohocken, PA https://doi.org/10.1520/E0003-11R17. [Link: ASTM International, https://store.astm.org/e0003-11r17.html]

[53] Manikandan P, Venkatesan K (2024) The influence of linear energy density on density, defect formation, residual stress, microstructure, and texture in 310 austenitic stainless steel by laser powder bed fusion. J Manuf Process 131:2191–2207. https://doi.org/10.1016/j.jmapro.2024.10.022

[54] Douglas R, Beard W, Barnard N, Lee S, Shao S, Shamsaei N, Jones T, Lancaster R (2024) The influence of energy density on the low cycle fatigue behaviour of laser powder bed fused stainless steel 316L. Int J Fatigue. https://doi.org/10.1016/j.ijfatigue.2023.108123

[55] Dowling L, Kennedy J, Trimble D (2022) Effect of a modified energy density equation to achieve a more uniform energy input during LPBF for improved repeatability. J Manuf Process 77:607–615. https://doi.org/10.1016/j.jmapro.2022.03.045

[56] Bakhtiarian M, Omidvar H, Mashhuriazar A, Sajuri Z, Gur CH (2024) The effects of SLM process parameters on the relative density and hardness of austenitic stainless steel 316L. J Mater Res Technol 29:1616–1629. https://doi.org/10.1016/j.jmrt.2024.01.237

[57] Sun Z, Tan X, Tor SB, Yeong WY (2016) Selective laser melting of stainless steel 316L with low porosity and high build rates. Mater Des 104:197–204. https://doi.org/10.1016/j.matdes.2016.05.035

[58] Zhang B, Li Y, Bai Q (2017) Defect formation mechanisms in selective laser melting: a review. Chin J Mech Eng 30:515–527. https://doi.org/10.1007/s10033-017-0121-5

[59] Zheng Z, Peng L, Wang D (2021) Defect analysis of 316 l stainless steel prepared by Lpbf additive manufacturing

processes. Coatings. https://doi.org/10.3390/coatings11121562

[60] Yang G, Xie Y, Zhao S, Qin L, Wang X, Wu B (2022) Quality control: internal defects formation mechanism of selective laser melting based on laser-powder-melt pool interaction: a review. Chinese J Mech Eng Addit Manuf Front 1(3):1–21. https://doi.org/10.1016/j.cjmeam.2022.100037

[61] Mukherjee T, DebRoy T (2018) Mitigation of lack of fusion defects in powder bed fusion additive manufacturing. J Manuf Process 36:442–449. https://doi.org/10.1016/j.jmapro.2018.10.028

[62] Ji C, Li K, Liao R, Li Z, Yin B, Wen P, Jiang B, Murr LE, Pan F (2025) Tensile creep mechanisms of laser powder bed fused WE43 alloy with heterogeneous microstructure: evolution in dislocations and precipitates. J Mater Sci Technol 238:209–229. https://doi.org/10.1016/j.jmst.2025.02.063

[63] Larimian T, Kannan M, Grzesiak D, AlMangour B, Borkar T (2020) Effect of energy density and scanning strategy on densification, microstructure and mechanical properties of 316L stainless steel processed via selective laser melting. Mater Sci Eng, A. https://doi.org/10.1016/j.msea.2019.138455

[64] Liu J, Wen P (2022) Metal vaporization and its influence during laser powder bed fusion process. Mater Des. https://doi.org/10.1016/j.matdes.2022.110505

[65] Shi G, Zhang R, Cao Y, Yang G (2024) A review of the vaporization behavior of some metal elements in the LPBF process. Micromachines. https://doi.org/10.3390/mi15070846

[66] Martucci A, Aversa A, Lombardi M (2023) Ongoing challenges of laser-based powder bed fusion processing of Al alloys and potential solutions from the literature: a review. Materials. https://doi.org/10.3390/ma16031084

[67] Wang D, Song C, Yang Y, Bai Y (2016) Investigation of crystal growth mechanism during selective laser melting and mechanical property characterization of 316L stainless steel parts. Mater Des 100:291–299. https://doi.org/10.1016/j.matdes.2016.03.111

[68] Yadroitsev I, Krakhmalev P, Yadroitsava I, Johansson S, Smurov I (2013) Energy input effect on morphology and microstructure of selective laser melting single track from metallic powder. J Mater Process Technol 213:606–613. https://doi.org/10.1016/j.jmatprotec.2012.11.014

[69] Leicht A, Fischer M, Klement U, Nyborg L, Hryha E (2021) Increasing the productivity of laser powder bed fusion for stainless steel 316L through increased layer thickness. J Mater Eng Perform 30:575–584. https://doi.org/10.1007/s11665-020-05334-3

[70] Pham MS, Dovgyy B, Hooper PA, Gourlay CM, Piglione A (2020) The role of side-branching in microstructure development in laser powder-bed fusion. Nat Commun. https://doi.org/10.1038/s41467-020-14453-3

[71] Sufiiarov VS, Popovich AA, Borisov EV, Polozov IA, Masaylo DV, Orlov AV (2017) The effect of layer thickness at selective laser melting. Procedia Eng 174:126–134. https://doi.org/10.1016/j.proeng.2017.01.179

[72] Chernyshikhin S, Fedorenko L, Egorov V, Zotov B, Brykin V, Korobov K, Nalivaiko A, Zherebtsov D, Lyange M, Pelevin I (2025) Laser powder bed fusion of AlSi10Mg with increased layer thickness for higher building rate. Int J Lightweight Mater Manuf. https://doi.org/10.1016/j.ijlmm.2025.07.010

[73] Shergill K, Chen Y, Bull S (2023) What controls layer thickness effects on the mechanical properties of additive manufactured polymers. Surf Coat Technol. https://doi.org/10.1016/j.surfcoat.2023.130131

[74] Cacace S, Pagani L, Colosimo BM, Semeraro Q (2022) The effect of energy density and porosity structure on tensile properties of 316L stainless steel produced by laser powder bed fusion. Prog Addit Manuf. https://doi.org/10.1007/s40964-022-00281-y

[75] Lou X, Andresen PL, Rebak RB (2018) Oxide inclusions in laser additive manufactured stainless steel and their effects on impact toughness and stress corrosion cracking behavior. J Nucl Mater 499:182–190. https://doi.org/10.1016/j.jnucmat.2017.11.036

[76] Deng P (2020) The origins of nanoscale oxide inclusion and its evolution in additively manufactured austenitic stainless steel during laser powder bed fusion and post heat treatment. PhD Thesis (Auburn University: Auburn)

[77] Eriksson P (2018) Evaluation of mechanical and microstructural properties for laser powder-bed fusion 316L. MSc Thesis (Uppsala Universitet, Uppsala)

[78] Montero Sistiaga ML, Nardone S, Hautfenne C, Humbeeck JV (2016) Effect of heat treatment of 316L stainless steel produced by selective laser melting (SLM). In: Proceedings of the solid freeform fabrication 2016: Proceedings of the 26th annual international, pp 560–565

[79] Montero-Sistiaga ML, Godino-Martinez M, Boschmans K, Kruth JP, Van Humbeeck JV, Vanmeensel K (2018) Microstructure evolution of 316L produced by HP-SLM (High Power Selective Laser Melting). Addit Manuf 23:402–410. https://doi.org/10.1016/j.addma.2018.08.028

[80] Yasa E, Deckers J, Kruth JP, Rombutus M, Luyten J (2009) Experimental investigation of Charpy impact tests on metallic SLM parts. In: Proceedings of the innovative

developments in design and manufacturing; CRC Publishers: Portugal, pp 207–214

[81] Röttger A, Boes J, Theisen W, Thiele M, Esen C, Edelmann A, Hellmann R (2020) Microstructure and mechanical properties of 316L austenitic stainless steel processed by different SLM devices. Int J Adv Manuf Technol 108:769–783. https://doi.org/10.1007/s00170-020-05371-1

[82] Luis González-Velázquez (2018) Fractography and failure analysis; Correia JAF 1st edn. vol 3. Springer: Mexico City

[83] ASTM E23-04 (2004) Standard test methods for notched bar impact testing of metallic materials, ASTM International, West Conshohocken https://doi.org/10.1520/E0023-04. [Link: ASTM International, https://store.astm.org/e0023-04.html]